

Lagrangian Coherent Structures and Vortex Formation in High Spatiotemporal-Resolution Satellite Winds of an Atmospheric Kármán Vortex Street

Tobias Günther^{1,1}, Akos Horvath^{2,2}, Wayne Bresky^{3,3}, Jaime Daniels^{3,3}, and Stefan Alexander Buehler^{4,4}

¹Friedrich-Alexander-University of Erlangen Nuremberg

²University of Hamburg

³National Oceanic and Atmospheric Administration (NOAA)

⁴Universität Hamburg

January 20, 2023

Abstract

Recent advances in geostationary imaging have enabled the derivation of high spatiotemporal-resolution cloud-motion winds for the study of mesoscale unsteady flows. Due to the general absence of ground truth, the quality assessment of satellite winds is challenging. In the current limited practice, straightforward plausibility checks on the smoothness of the retrieved wind field or tests on aggregated trends such as the mean velocity components are applied for quality control. In this paper, we demonstrate additional diagnostic tools based on feature extraction from the retrieved velocity field. Lagrangian Coherent Structures (LCS), such as vortices and transport barriers, guide and constrain the emergence of cloud patterns. Evaluating the alignment of the extracted LCS with the observed cloud patterns can potentially serve as a test of the retrieved wind field to adequately explain the time-dependent dynamics. We discuss the suitability and expressiveness of direct, geometry-based, texture-based, and feature-based flow visualization methods for the quality assessment of high spatiotemporal-resolution winds through the real-world example of an atmospheric Kármán vortex street and its laboratory archetype, the 2D cylinder flow.

1 **Lagrangian Coherent Structures and Vortex Formation**
2 **in High Spatiotemporal-Resolution Satellite Winds of**
3 **an Atmospheric Kármán Vortex Street**

4 **T. Günther¹, Á. Horváth², W. Bresky³, J. Daniels⁴, and S. A. Buehler²**

5 ¹Friedrich-Alexander-Universität Erlangen-Nürnberg, Erlangen, Germany

6 ²Meteorological Institute, Universität Hamburg, Hamburg, Germany

7 ³I. M. Systems Group, Rockville, MD, USA

8 ⁴NOAA/NESDIS Center for Satellite Applications and Research, College Park, MD, USA

9 **Key Points:**

- 10 • Recently developed high-cadence geostationary satellite winds enable the Lagrangian
11 analysis of unsteady island wake flows
- 12 • The good correspondence between the derived Lagrangian Coherent Structures
13 and the observed cloud patterns indirectly confirms the fidelity of the fluid dynam-
14 ics embedded in the satellite winds
- 15 • Spatial verification metrics that compare measured with simulated Lagrangian flow
16 features can complement traditional gridpoint-based statistics in quantitative model
17 validation

Corresponding author: Tobias Günther, tobias.guenther@fau.de

Abstract

Recent advances in geostationary imaging have enabled the derivation of high spatiotemporal-resolution cloud-motion winds for the study of mesoscale unsteady flows. Due to the general absence of ground truth, the quality assessment of satellite winds is challenging. In the current limited practice, straightforward plausibility checks on the smoothness of the retrieved wind field or tests on aggregated trends such as the mean velocity components are applied for quality control. In this paper, we demonstrate additional diagnostic tools based on feature extraction from the retrieved velocity field. Lagrangian Coherent Structures (LCS), such as vortices and transport barriers, guide and constrain the emergence of cloud patterns. Evaluating the alignment of the extracted LCS with the observed cloud patterns can potentially serve as a test of the retrieved wind field to adequately explain the time-dependent dynamics. We discuss the suitability and expressiveness of direct, geometry-based, texture-based, and feature-based flow visualization methods for the quality assessment of high spatiotemporal-resolution winds through the real-world example of an atmospheric Kármán vortex street and its laboratory archetype, the 2D cylinder flow.

1 Introduction

Vortex streets formed in the cloudy wake of mountainous islands are the analogues of the classic Kármán vortex street observed in laboratory bluff-body flows. Atmospheric vortex streets develop in conditions characterized by a well-mixed subcloud layer capped by a strong temperature inversion with a weaker stably stratified layer above and consist of mesoscale eddies, which span the entire marine boundary layer and have a nearly upright axis with no height variation in their properties (i.e. they are approximately 2D). Although the spatial arrangement (aspect ratio) of these spectacular vortex patterns has been studied ever since their first photographs were obtained at the dawn of the satellite era (e.g. Chopra & Hubert, 1965; Hubert & Krueger, 1962; Lyons & Fujita, 1968; Young & Zawislak, 2006), advances in modeling and observational capabilities have recently led to a renewed interest specifically in their dynamics. Numerical forecast models and large-eddy simulations are now capable of handling spatial grid resolutions at the lower end of the meso-gamma scale (2–20 km) in a sufficiently large domain (hundreds of kilometers on a side) required for the realistic modeling of island wakes (Nunalee & Basu, 2014; Nunalee et al., 2015; Heinze et al., 2012).

The spatial resolution of satellite wind retrievals has also reached the kilometer scale (2–8 km), at least in a research setting if not operationally, which allows to characterize the finer details of wake flows. The wind and vorticity field of atmospheric vortex streets was successfully measured by stereo cloud-motion winds from the Multiangle Imaging SpectroRadiometer (MISR; Horváth (2013)) and also by ocean surface winds from the Advanced Scatterometer (ASCAT; Vogelzang et al. (2017)). These polar-orbiter instruments, however, only offer snapshots of the wind field. The latest generation geostationary imagers, in contrast, can provide high-cadence wind retrievals that capture the time evolution of the wake. Horváth et al. (2020) used the Advanced Baseline Imager (ABI) aboard Geostationary Operational Environmental Satellite-16 (GOES-16) to derive 6-km resolution cloud-motion winds at 5-min frequency, to characterize the wake oscillations and to measure vortex shedding, advection, and decay in the lee of Guadalupe Island.

High spatiotemporal-resolution winds represent both challenges and opportunities. The validation of satellite winds is difficult due to the general lack of ground truth and traditionally relies on comparisons against sparse radiosonde observations. In recent years, aircraft observations have also been used to evaluate derived winds, but even with this additional data source there are significant gaps in the in-situ measurement network. As a result, the quality control of operational satellite winds mostly relies on spatial and

69 temporal self-consistency checks. The quality of retrievals is expressed by the level of vec-
70 tor, speed, and direction consistency between neighboring as well as between consecu-
71 tive wind vectors (Holmlund et al., 2001). These quality control schemes were designed
72 with coarser-resolution global forecast models in mind, which require a description of the
73 slowly varying large-scale flow. They are, however, inapplicable to unsteady wake flows
74 that are characterized by large wind variations on small spatial and temporal scales, due
75 to both small-scale dynamics and measurement uncertainties. Furthermore, the obser-
76 vation of local wind vectors alone does not allow flow comparison on the scale of features
77 such as vortices, as soon as those are in motion, because of the superimposed transport (Günther
78 & Theisel, 2018).

79 The effective visualization of high-resolution winds is also challenging. Traditional
80 vector plots (wind barbs or arrows) are unsuitable for time-dependent flow, due to their
81 inability to separate features from the underlying motion. In addition, spatially dense
82 datasets suffer from occlusion of vectors. There are, however, alternative techniques that
83 are similarly easy to calculate, yet are more informative, as they reveal underlying trans-
84 port dynamics much more clearly. For example, a user survey of 2D vector field visu-
85 alization methods found that techniques representing integral curves and conceptualiz-
86 ing particle advection tend to perform better in time-varying flows (Laidlaw et al., 2005).
87 Recently, Bujack and Middel (2020) pointed out that atmospheric flows are visualized
88 almost exclusively by basic techniques only (arrows, streamlines, or color coding the ve-
89 locity magnitude) and recommended the more regular use of feature-based methods.

90 The goal of the current study, a follow-on to Horváth et al. (2020), is to demon-
91 strate the opportunities for progress on both of these fronts. Complex spatiotemporal
92 systems such as atmospheric vortex streets are highly structured, but nevertheless or-
93 ganize around a lower-dimensional skeleton of coherent features. We investigate selected
94 techniques from direct, geometric, image-based, and feature-based flow visualization re-
95 garding their potential to serve as diagnostic measure, leading up to Lagrangian Coher-
96 ent Structures (LCS; Haller, 2015), which identify the most attracting, repelling, and shear-
97 ing material lines of particle dynamics. Such material boundaries, which can now be cal-
98 culated thanks to the high-frequency of ABI winds, are of interest, because they segment
99 the flow into compartments of coherent behavior. We show that LCS and particle/texture
100 advection methods applied to the Guadalupe wind data well describe the emergence of
101 the observed cloud vortex patterns and thus indirectly confirm the quality of the satel-
102 lite wind retrievals. We argue that these techniques might serve as complementary tools
103 for the validation, or at least consistency testing, and visualization of high spatiotemporal-
104 resolution wind data. The atmospheric vortex street is a good case study, because we
105 can also draw on and compare against well-known results obtained by the above tech-
106 niques for the classic 2D cylinder flow.

107 The paper is organized as follows. In Section 2, we introduce the notation used and
108 briefly describe our measurement and simulation data. Section 3 describes the pitfalls
109 of direct visualization methods, such as arrow plots. Section 4 elaborates on the calcu-
110 lation and use of geometric visualization methods that are centered around particle in-
111 tegration. Section 5 increases the information density by image-based techniques such
112 as line integral convolutions. Section 6 takes a feature-centered approach to visualize the
113 coherent structures in fluid flow. Finally, Section 7 concludes with an outline of oppor-
114 tunities for future work.

115 In the supplemental material, we provide a Matlab implementation of the feature
116 extraction methods explained throughout the paper, scripts to reproduce the Matlab-
117 generated figures, as well as links to the data sets in netCDF format. In addition, the
118 supplemental material contains time series animations of the different visualization meth-
119 ods.

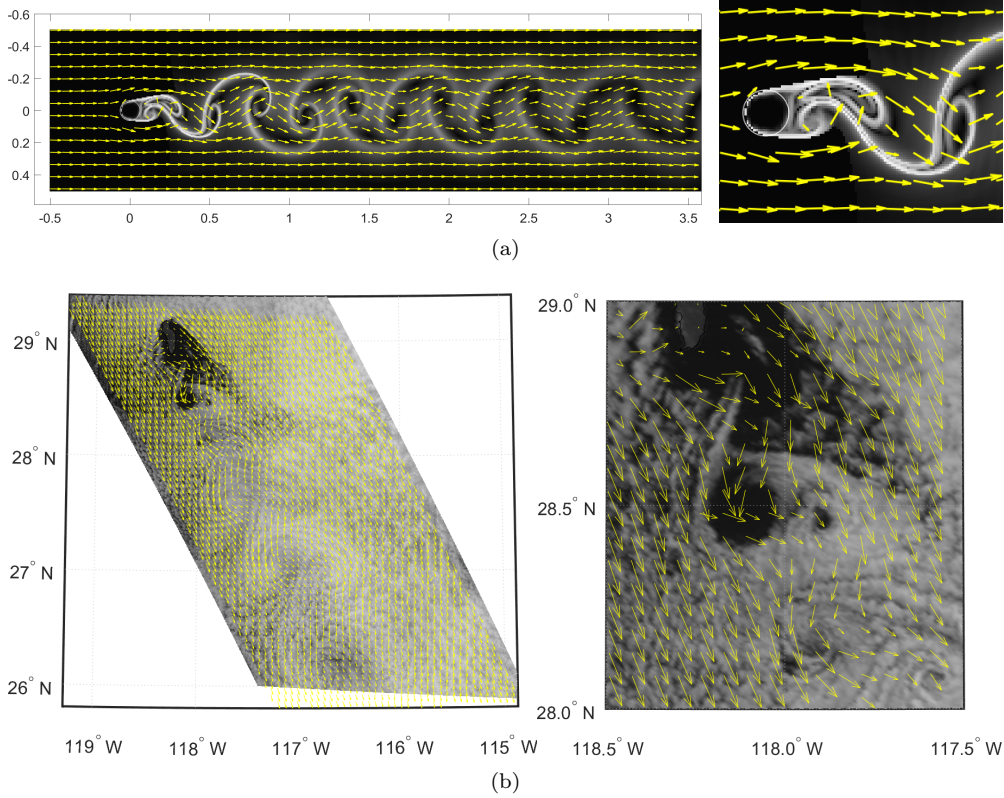


Figure 1: Arrow plots of the CYLINDER2D flow at $t = 7.5$ (a) and the GUADALUPE flow at 17:03 UTC (b). The left image shows the full domain and the right image presents a close-up view of the leeward side of the obstacle.

2 Background and Data

2.1 Notation

Throughout this work, we will refer to scalar numbers with italic letters, such as s . Vector-valued quantities are expressed with bold letters, such as \mathbf{v} . Matrices are denoted with capitalized bold letters, such as \mathbf{J} .

A vector field is a map $\mathbf{v}(\mathbf{x}, t) = \mathbf{v}(x, y, t) : D \times T \rightarrow D$ that assigns each point $\mathbf{x} \in D$ in the *two-dimensional* domain $D \subset \mathcal{R}^2$ a vector:

$$\mathbf{v}(x, y, t) = \begin{pmatrix} u(x, y, t) \\ v(x, y, t) \end{pmatrix} \quad (1)$$

If \mathbf{v} depends on time it is called *unsteady* or time-dependent. Otherwise, the flow is called *steady*, i.e., when the time partial derivative vanishes to zero: $\frac{\partial}{\partial t} \mathbf{v} = \mathbf{0}$.

We explain all visualization methods through the examples of (i) a numerically-simulated 2D vector field of the classic cylinder flow and (ii) a satellite-retrieved real-world quasi-2D meteorological vector field containing an atmospheric Kármán vortex street. In the following, we give a brief description of the data sets and explain the first visualization method.

132

2.2 Data Sets

133

134

135

136

137

138

139

140

141

142

143

144

145

146

CYLINDER2D Flow. For reference, we apply the visualization methods to the well-known laboratory Kármán vortex street. This fluid flow was numerically simulated with the open source solver Gerris (Popinet, 2003). The spatial domain $[-0.5, 7.5] \times [-0.5, 0.5]$ is filled with a viscous 2D fluid that is injected from the left into a channel with solid walls and slip boundary conditions. A circular obstacle is placed at $(0, 0)$ with radius 0.0625. The kinematic viscosity is $\nu = 0.00078125$, leading to a Reynolds number of $Re = 160$. The data set is discretized onto a 640×80 grid and the time range $[0, 15]$ is discretized with 1501 time steps. The velocity vector field is publicly available; for more details on its definition we refer to Günther et al. (2017). Fig. 1a shows the periodic patterns forming in the wake of the cylinder. Arrows do not align with the flow structures (shown in white), which are instead revealed by visualizing structures that tracer particles are attracted to, i.e., locations at which smoke would collect if it was released from the cylinder. The white structures are calculated by the (backward) finite-time Lyapunov exponent, which is explained later.

147

148

149

150

151

152

153

154

155

156

157

158

159

160

161

162

163

164

GUADALUPE Flow. Satellite cloud-motion vectors (or "winds") were derived for the atmospheric Kármán vortex street observed by GOES-16 in marine stratocumulus in the lee of Guadalupe Island off Baja California on 9 May 2018. The stratocumulus deck was located above a low-level temperature inversion starting at a base height of 570 m, with cloud top heights varying between 600 and 900 m and having a median value of 750 m. The cloud-motion vectors thus represent horizontal winds within a narrow layer (at a nearly constant level) and were extracted from 0.5-km resolution red band ($0.64\text{-}\mu\text{m}$) imagery provided by ABI every 5 min. Retrievals were generated from consecutive image pairs for the 8-hour period between 14:32–22:37 UTC, totaling 96 time steps and covering a 602×602 -pixel domain encompassing Guadalupe and its wake down to 26°N latitude. A 5×5 -pixel ($\sim 2.5 \times 2.5 \text{ km}^2$) subscene was centered on each pixel in this domain and tracked forward in time by minimizing the sum of squared difference similarity measure between the target image subscene and the search image subscene (Bresky et al., 2012; Daniels et al., 2010). The resulting 2.5-km resolution local winds were then resampled onto a Universal Transverse Mercator (UTM) grid with a spacing of 6.3 km. To reduce noise, each UTM gridbox was assigned the median of the local wind vectors it contained. For more details, including a public link to the data repository, see Horváth et al. (2020).

165

166

167

168

169

170

171

172

173

174

175

176

An arrow plot of the island wake is shown in Fig. 1b. Note that the arrows do not reveal the mushroom patterns visible in the clouds, since the arrow direction depends not only on the local motion indicated by the vortex pattern but also on its transport. Namely, the arrow direction is a superposition of flow features (e.g., vortical motion inside vortices) and the ambient transport (overall transport tendency). Thus, arrows are unsuitable to study the correlation with the observed imagery. The satellite-retrieved data exhibit occasional outliers with exceptionally high wind speed and strong deviation from surrounding vectors. In Horváth et al. (2020), the vertical component of relative vorticity calculated from the horizontal winds was smoothed with a simple 3×3 -gridbox averaging window to reduce the effect of outliers. In the current paper, we preprocess the flow in a more sophisticated manner in order to be able to apply visualization methods that require the numerical estimation of derivatives.

Let \mathcal{D} be the spatial domain of the data and let $\mathcal{M} \subset \mathcal{D}$ be the part of the domain in which the velocity values are available and not marked as outlier, i.e., the absolute value of both velocity components is below 8 m/sec , a threshold we chose empirically. Given the original vector field $\mathbf{v}(\mathbf{x}, t)$ at each given time t , we minimize the fol-

lowing energy E to solve for a new vector field $\mathbf{v}^*(\mathbf{x}, t)$ such that

$$E = \underbrace{\int_{\mathcal{M}} \|\mathbf{v}(\mathbf{x}, t) - \mathbf{v}^*(\mathbf{x}, t)\|^2 \partial\mathbf{x}}_{\text{data similarity}} + \lambda \underbrace{\int_D \left\| \frac{\partial \mathbf{v}^*(\mathbf{x}, t)}{\partial \mathbf{x}} \right\|^2 \partial\mathbf{x}}_{\text{smoothness}} \rightarrow \min \quad (2)$$

177 Since the above energy is quadratic in its unknowns, it has one optimal solution that can
 178 be found by discretizing the domain and performing a linear least squares fit. Here, we
 179 fit a vector field to the satellite winds, wherever they are available, and we generally as-
 180 sume that the desired vector field is smooth, which is known as Tikhonov regularization.
 181 The parameter λ is thereby a smoothness weight, which we empirically set to $\lambda = 0.2$.

182 3 Direct Methods

183 Direct visualization methods encode components of the vector field by color or place
 184 glyphs at discrete locations to convey derived information. For general vector field data,
 185 the most commonly used glyph is an arrow that depicts the wind direction; for the spe-
 186 cial case of meteorological wind fields an alternative is the wind barb. For a compre-
 187 hensive introduction to glyph-based techniques, we refer to the survey of Borgo et al. (2013).

188 3.1 Arrow Plots

189 Arrow plots visualize a vector field by placing a small arrow at each data grid point,
 190 indicating the direction of the flow using the arrow direction and the magnitude of the
 191 vector by the length of the arrow. Examples can be seen in Fig. 1. Care must be taken
 192 not to make the arrows too long, as they start to overlap otherwise. Because the exact
 193 magnitude might be difficult to discern when viewing vectors, meteorologists often pre-
 194 fer the use of wind barbs, which consist of a fixed-length shaft indicating direction and
 195 a combination of short and long barbs and pennants (collectively 'feathers') to indicate
 196 speed. Wind barb overlap, however, is even more of an issue for dense vector fields, due
 197 to the presence of the 'feathers'. In interactive visualization applications, the number
 198 of arrows can be increased when the user zooms in to maintain a constant arrow den-
 199 sity.

200 3.2 Discussion

An arrow plot is generally ineffective in showing a time-dependent fluid flow phe-
 nomenon. In Fig. 1a, for instance, the location of vortices and other fluid flow features
 is not apparent from the visualization. Arrow plots can therefore not form the basis of
 conclusions about flow behavior. The continuum mechanical reason for this is that the
 physical interpretation of the vector orientation and length is not *objective* (Truesdell
 & Noll, 1965). Intuitively, lacking objectivity means that two different observers, for ex-
 ample one standing still and another one performing a rotation, might draw different con-
 clusions when observing the same physical phenomenon, which is highly undesirable. Ob-
 jectivity is a mathematical property that is obtained when a measure is invariant un-
 der uniform rotations and translations of the reference frame, i.e., all observers will draw
 the same conclusion. Formally, let $\mathbf{v}(\mathbf{x}, t)$ be a vector-valued property observed in frame
 \mathcal{F}_1 and $\mathbf{w}(\mathbf{y}, t)$ be the same vector-valued property observed in frame \mathcal{F}_2 that is mov-
 ing relative to \mathcal{F}_1 by a Euclidean transformation:

$$\mathbf{y} = \mathbf{Q}(t)\mathbf{x} + \mathbf{c}(t), \quad (3)$$

where $\mathbf{Q}(t)$ is an arbitrary time-dependent rotation matrix, and $\mathbf{c}(t)$ is an arbitrary time-
 dependent translation vector. Then, the vector-valued property is objective if it fulfills:

$$\mathbf{w}(\mathbf{y}, t) = \mathbf{Q}\mathbf{v}(\mathbf{x}, t). \quad (4)$$

201 Since arrow length and orientation are different for differently moving observers, arrows
 202 are not useful to study the behavior of particles in the fluid and their immediate value
 203 as quality metric in a vector field comparison is limited. Arrow plots can only reveal in-
 204 stantaneous structures, as for example needed in streamline-oriented topology (Günther
 205 & Baeza Rojo, 2021). Nevertheless, an arrow plot is a frequent first choice to get an ini-
 206 tial impression of the vector data, for example to investigate the amount of noise present
 207 at individual grid points. A more sensible quality metric would inspect reference frame
 208 invariant features that are derived from the velocity field and would utilize the tempo-
 209 ral coherence of those structures. In the following section, we take the first step in this
 210 direction by inspecting integral geometry that reveals patterns and may serve as struc-
 211 ture along which coherence can be measured.

212 4 Geometric Methods

213 4.1 Flow Maps

214 In experimental flow visualization, a common approach to visualize a usually in-
 215 visible fluid flow is to release tracers such as smoke or dye or hydrogen bubbles, which
 216 are advected by the flow, creating striking patterns (streaklines) that convey the motion
 217 of the fluid (Van Dyke, 1982). In atmospheric flows, this is partially mimicked by the
 218 observation of clouds, though their evolution is not strictly a matter of passive advec-
 219 tion. Once vector fields are captured or numerically simulated, computational flow vi-
 220 sualization provides a multitude of approaches to visualize the fluid flow structures, which
 221 identify the driving processes that govern the transport. We thereby distinguish between
 222 Eulerian approaches that analyze the flow per time step and Lagrangian approaches that
 223 derive an analysis from particle motion. Therefore, a key ingredient is the ability to trace
 224 virtual particles, which we cover below.

In an *unsteady* flow $\mathbf{v}(\mathbf{x}, t)$, i.e., when the flow is changing over time, the trajec-
 tory $\mathbf{x}(t)$ of a massless tracer particle is called a *pathline*. For a given seed point \mathbf{x}_0 and
 seed time t_0 , a pathline is the solution to the ordinary differential equation (ODE):

$$\frac{d}{dt}\mathbf{x}(t) = \mathbf{v}(\mathbf{x}(t), t) \quad \text{with} \quad \mathbf{x}(t_0) = \mathbf{x}_0. \quad (5)$$

i.e., the pathline is always tangential to the flow. The trajectory is numerically calcu-
 lated as an initial value problem for a given initial condition using:

$$\mathbf{x}(t) = \mathbf{x}(t_0) + \int_{t_0}^t \mathbf{v}(\mathbf{x}(\tau), \tau) d\tau \quad \text{with} \quad \mathbf{x}(t_0) = \mathbf{x}_0. \quad (6)$$

225 In an unsteady flow, each particle needs to store its current position and also its current
 226 time, since the vector field that describes where the particles goes next is time-dependent.

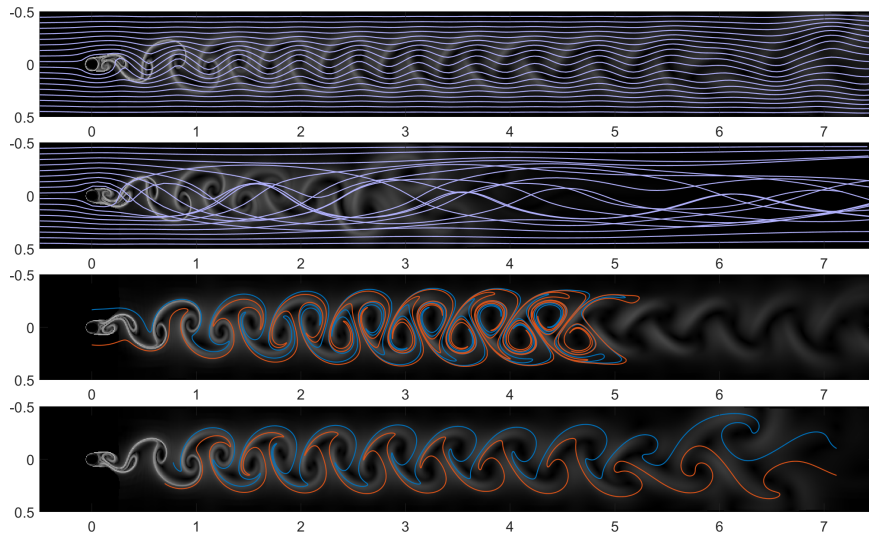
For notational convenience, it is common to introduce the *flow map* $\Phi_{t_0}^\tau(\mathbf{x}_0) : D \rightarrow D$, which maps a particle seeded at location \mathbf{x}_0 at time t_0 to its destination after path-
 line integration for duration τ , cf. Haller (2015):

$$\Phi_{t_0}^\tau(\mathbf{x}_0) = \mathbf{x}_0 + \int_{t_0}^{t_0+\tau} \mathbf{v}(\mathbf{x}(t), t) dt. \quad (7)$$

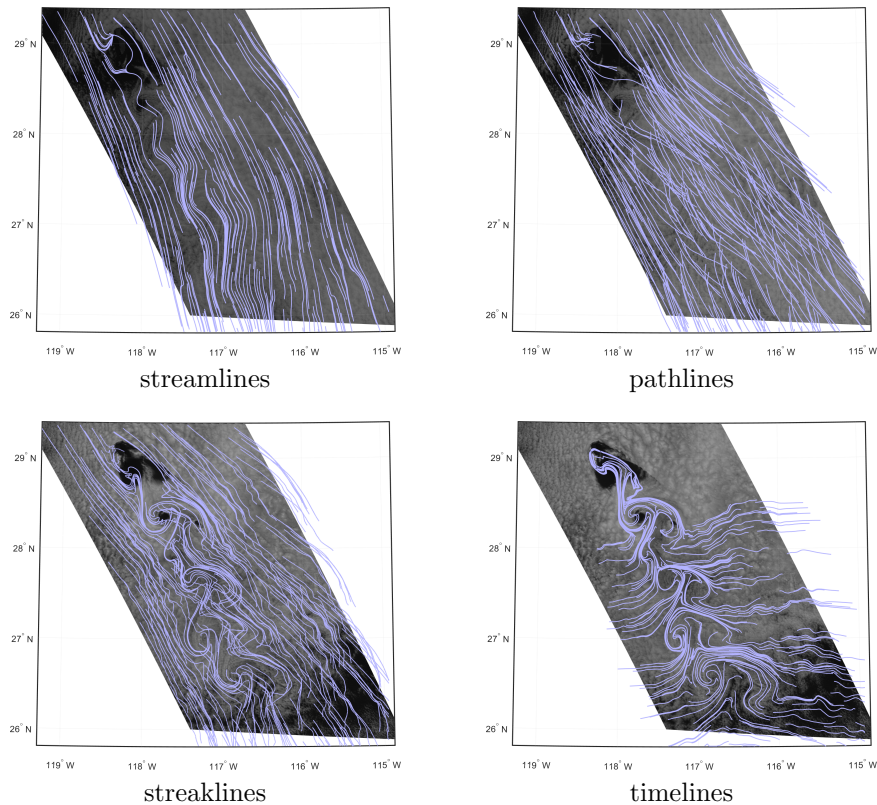
227 The flow map is rarely visualized directly. Instead structures and features are derived
 228 from it, which enables more quantification and measurements, for instance for the de-
 229 tection of transport barriers and vortices. We will describe those approaches later in more
 230 detail.

231 4.2 Integral Curves

232 Throughout the flow visualization literature, we can find a number of different line
 233 geometries that are used to study particle motion (McLoughlin et al., 2010). The tra-



(a)



(b)

Figure 2: In (a), we see integral curves in the CYLINDER2D flow, from top to bottom: streamlines ($t_0 = 10$, $\tau = 9$), pathlines ($t_0 = 6$, $\tau = 9$), streaklines ($t_0 = 7$, $\tau = 5$) and timelines ($t_0 = 8$, $\tau = 1.2$). Streaklines and timelines align with the flow patterns in the background. In (b), integral curves of the GUADALUPE flow are shown ($t_0 = 15:55:20$ UTC, $\tau = 06:06:40$ UTC) with satellite images in the background (for streamlines and pathlines at start time t_0 , and for streaklines and time lines at end time $t_0 + \tau$).

234 jectories of particles in a fluid flow are generally referred to as integral (or characteris-
 235 tic) curves, referring to the integral formulation of the ODE that defines them, see for
 236 example Eq. (6). Depending on the type of fluid flow—steady or unsteady—different kinds
 237 of integral curves arise that have different meaning. In geometry-based flow visualiza-
 238 tion, we primarily distinguish four types of integral curves, which are illustrated in Fig. 2a
 239 for the flow behind a CYLINDER and in Fig. 2b for the GUADALUPE flow. In both cases,
 240 we would like a Kármán vortex street to appear. In the following, we will investigate how
 241 well the various types of integral curves are able to reveal this flow pattern.

- 242 • *Streamlines* are the tangent curves of steady vector fields, i.e., $\frac{d}{dt}\mathbf{r}(t) = \mathbf{v}(\mathbf{r}(t))$
 243 where $\mathbf{v}(\mathbf{x})$ is a steady (time-independent) vector field or a time slice of an un-
 244 steady flow. Usually, they are used to study instantaneous vector fields such as
 245 magnetic fields or truly steady flows. In a time-dependent flow, they are calcu-
 246 lated per time slice, which is not physically meaningful. Since actual particles move
 247 forward in time, i.e., the flow is temporally changing as the particles are travel-
 248 ing, streamlines do not correspond to the physical trajectory of a real particle. When
 249 plotting streamlines in an unsteady flow, flow patterns such as vortices might be-
 250 come apparent. It should, however, always be clear that these structures do not
 251 actually exist and they should not be the foundation of an argumentation in flow
 252 analysis.
- 253 • *Pathlines* were defined as the solution to an initial value problem in Eq. (6). Us-
 254 ing the flow map in Eq. (7), they are given by $\mathbf{p}(\tau) = \Phi_{t_0}^\tau(\mathbf{x}_0)$ and describe the
 255 paths of massless particles in fluid flows. These lines are in fact the trajectories
 256 of individual particles and are therefore the preferred choice when studying trans-
 257 port properties in time-dependent vector fields. Similar to streamlines, these lines
 258 are the result of an ODE, cf. Eq. (5). Note how neither streamlines nor pathlines
 259 are able to reveal the vortex street in the fluid flows. While it is generally not mean-
 260 ingful to view streamlines in time-dependent flows, it is not enough either to view
 261 pathlines when looking for flow patterns. A pathline is a series of locations that
 262 have been visited by a given particle at *different* moments in time. Pathlines are
 263 therefore not useful to depict flow patterns at *one* specific moment in time.
- 264 • *Streaklines*, on the other hand, are used to reveal flow patterns at *one* specific mo-
 265 ment in time. They are assembled by continuously releasing particles from a seed
 266 point \mathbf{x}_0 at different times and advecting all particles to the same time slice, which
 267 is referred to as the observation time t . Using the flow map in Eq. (7), streaklines
 268 are defined as $\mathbf{s}(\tau) = \Phi_\tau^{t-\tau}(\mathbf{x}_0)$. Conceptually, streaklines are the equivalent to
 269 the trail of smoke or ink released from a point source, which takes us much closer
 270 to experimental flow visualization methods. Note that streaklines are successful
 271 in revealing fluid flow patterns such as vortices, as long as the particles can reach
 272 those structures. Unlike streamlines and pathlines, which are computed by advect-
 273 ing a single particle, streaklines are computed by advecting a continuously grow-
 274 ing list of particles forward in time. Whenever two subsequent particles are rapidly
 275 moving apart from each other, a new particle has to be inserted in-between them
 276 in order to maintain a sufficiently fine discretization of the streakline. Ideally, the
 277 new particle is inserted at the seed point and is traced up to the observation time.
 278 For simplicity, however, it is common to interpolate the new particle location at
 279 the observation time from the two particles that drifted too far apart, which is eas-
 280 ier since it does not require access to previous time steps, but also introduces in-
 281 terpolation errors.
- 282 • *Timelines* are curves that are advected over time. For a seeding curve $\mathbf{c}(u)$ at time
 283 t_0 , the timeline at observation time $t_0 + \tau$ is $\mathbf{t}(u) = \Phi_{t_0}^\tau(\mathbf{c}(u))$. Conceptually,
 284 timelines correspond to a line of ink that is injected at only one moment in time
 285 and then advected to the observation time. Similar to streaklines, particles on a
 286 timeline may separate away from each other, which requires an adaptive refine-
 287 ment. Both streaklines and timelines reveal physically-meaningful flow patterns.

288 The main difference between streaklines and timelines is in the analysis question
 289 they answer: how do particles evolve that were seeded at different times but from
 290 the same location (streaklines) versus how do particles evolve that were seeded
 291 at the same time but from different locations (timelines).

292 Pathlines, streaklines, and timelines are computed for unsteady vector fields only, whereas
 293 streamlines can be computed for steady flows as well as for the individual time steps of
 294 unsteady flows. Note that streamlines, pathlines, and streaklines are identical in a steady
 295 vector field. It is worth mentioning that similar to streamlines, streaklines and timelines
 296 can also be calculated as tangent curves in a lifted higher-dimensional vector field com-
 297 puted from the spatial and temporal gradients of the flow map (Weinkauff et al., 2012).

298 When visualizing line geometry, we generally aim for less line intersections (in 2D)
 299 and less line occlusions (in 3D) in order to avoid visual clutter (Günther et al., 2017).
 300 An advantage of streamlines is that they cannot intersect, since only one trajectory can
 301 pass through each point in the domain. When pathlines are plotted in space they can
 302 intersect, since particles may pass through the same location at different times from a
 303 different direction. We can observe such intersections in Fig. 2. Streaklines will only in-
 304 tersect if a streakline sweeps over the seed point of another streakline. Self-intersections
 305 are also possible when the streakline particles move over their own seed point. Finally,
 306 timelines will intersect when their seed curves intersect.

307 When using line geometry to reveal flow patterns, we not only need an integration
 308 algorithm, but we also need a good seed placement or line selection algorithm in order
 309 to avoid the aforementioned intersections and occlusions. Generally, these approaches
 310 are categorized into density-based (Jobard & Lefer, 1997; Mattausch et al., 2003) meth-
 311 ods that evenly fill the domain with lines, feature-based (Ye et al., 2005; Yu et al., 2012)
 312 methods that place lines primarily around points of interest to ensure their visibility, and
 313 similarity-based (Chen et al., 2007) methods that avoid redundant lines that carry no
 314 additional information. We refer to Sane et al. (2020) for a recent survey.

315 4.3 Discussion

316 The various types of integral geometry have different strengths and weaknesses and
 317 should be applied accordingly. Shared among all types of geometry is the seeding prob-
 318 lem and the potential visual clutter when showing too many lines. Streamlines and path-
 319 lines are not suitable when searching for coherent structures, as they cannot reveal cloud
 320 patterns. While streaklines are preferred in this case, they have the downside that the
 321 time and place of formation of the revealed structures is unclear. For example, the streak-
 322 lines in Fig. 2a show more structure further downstream than directly behind the cylin-
 323 der. This is because the structures have accumulated over the life time of the particles.
 324 Once a structure has formed it will be advected further down the flow, making it unclear
 325 whether the implied rotating motion is still ongoing or whether the structure has been
 326 advected only. Timeline particles, on the other hand, have all been advected for the same
 327 amount of time, making the structures more comparable.

328 As Cimbala et al. (1988) pointed out, early experimental studies of bluff body wakes
 329 based on streakline photographs often arrived at erroneous conclusions about the local
 330 flow conditions due to this integrated memory effect. In order to accurately discern the
 331 flow at some location, the tracer source (smoke-wire, hydrogen bubble generator, or dye)
 332 must be placed at just the right distance upstream of that location (aka the seeding prob-
 333 lem). If the source is too close to the observation point, the streaklines do not have enough
 334 time to deform. Likewise if the source is too far upstream, the streakline pattern gets
 335 fixed and simply advects along with the mean flow. Laboratory streakline photographs
 336 may show well-defined vortex pairs far downstream of the obstacle, even though the lo-
 337 cal flow is nearly parallel. This is because vorticity decays at a much faster rate than smoke

338 or dye diffuses. A similar disconnect between the visual appearance of far-wake cloud
 339 vortex patterns and vorticity also affects the Guadalupe flow, see later Section 6.

340 An additional issue is line intersection. Streamlines can never intersect. Pathlines
 341 will intersect frequently, since they are assembled by particles living in different time steps.
 342 Streaklines will (self-)intersect whenever a streakline is advected over the seed point of
 343 another streakline—which is guaranteed to happen in any basic visualization tool with-
 344 out careful seed placement and streakline truncation—, and timelines will intersect when
 345 their initial seed curves intersect. The visual clutter caused by line intersection can be
 346 mitigated by truncating lines if their distance falls below a certain threshold.

347 5 Image-based Methods

348 The previous geometry-based methods require the seeding of line geometry. Even
 349 when placing lines with an even spacing between them, there is still empty space between
 350 lines for which the flow behavior is not visualized, potentially missing out details. In the
 351 following, texture-based methods are described, which encode information at every out-
 352 put pixel.

353 5.1 Texture Advection

A common approach to observe air and liquid flows in experimental flow visual-
 ization is by dye injection. Computationally, this can be reproduced by advecting a scalar
 field. The computational setting, however, allows us to inject patterns leading to more
 expressiveness. Since this advection is usually done on graphics processing units (GPUs),
 where scalar fields are best represented in texture memory, this technique is also known
 by the name texture advection. More formally, we can express the texture advection of
 a scalar field $s(\mathbf{x})$ with the flow map $\Phi_{t_0}^t(\mathbf{x})$, cf. Section 4.1, by using

$$s(\mathbf{x}, t) = s(\Phi_{t_0}^{t_0-t}(\mathbf{x})) \quad (8)$$

354 which results in the time-dependent scalar field $s(\mathbf{x}, t)$, which is equal to the initial tex-
 355 ture at $t = t_0$. Conceptually, there are many different ways to implement the advec-
 356 tion, such as numerically solving it as a partial differential equation (MacCormack, 2002),
 357 which would also allow for the modeling of effects like dissipation, or by taking a Lagrangian
 358 approach that advects a particle backwards to the seed time and fetches the texture value,
 359 as done in Eq. (8). The latter method is illustrated in Fig. 3, which is able to deform
 360 the texture, here a simple checkerboard pattern, without numerical dissipation. The black
 361 regions show locations from which the backward particle integration in Eq. (8) left the
 362 flow domain. The deformation of individual squares becomes quickly apparent as they
 363 stretch under the repelling flow and roll up into vortices. In fact, structures emerge even
 364 when a noise texture is advected with the flow. Using patterns such as the checkerboard,
 365 we can also see where no deformation has occurred, which is less obvious in previous vi-
 366 sualization methods. Note that edges in the checkerboard are timelines of the flow.

367 5.2 Line Integral Convolution

The line integral convolution (LIC) (Cabral & Leedom, 1993) is among the most
 common flow visualization methods, which is used to visualize the streamlines of a steady
 vector field $\mathbf{v}(\mathbf{x})$. Given a texture $T(\mathbf{x})$ with random noise values in $[0, 1]$ and a convo-
 lution kernel $k(s)$ with a support in $s \in [-l, l]$, the line integral convolution computes
 a gray value image $I(\mathbf{x}_0)$ for every point \mathbf{x}_0 in the domain:

$$I(\mathbf{x}_0) = \int_{s_0-l}^{s_0+l} k(s - s_0) \cdot T(\mathbf{s}(s)) \, ds \quad (9)$$

368 where $\mathbf{s}(s)$ is the streamline released at \mathbf{x}_0 that is traced in forward and backward di-
 369 rection for length l . Examples are shown in Fig. 4 (a)–(b). Conceptually, the LIC inte-

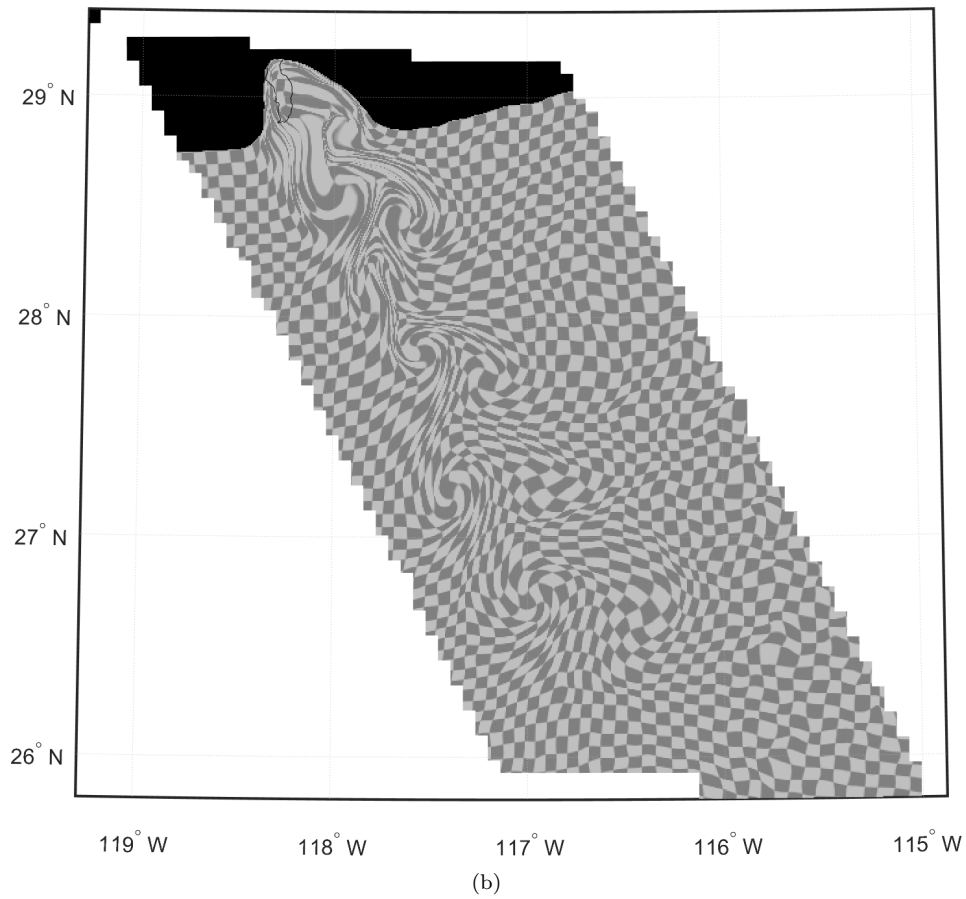
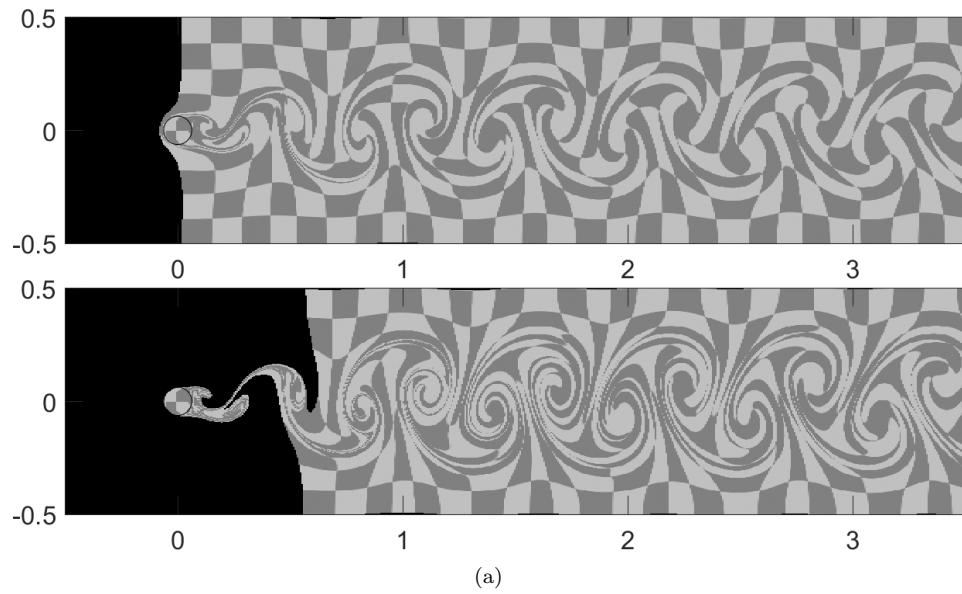


Figure 3: Texture advection of a checkerboard pattern reveals how patches deform during advection. In (a), CYLINDER2D flow from $t_0 = 10$ for duration $\tau = 0.5$ (top) and $\tau = 1.0$ (bottom). In (b), GUADALUPE flow from $t_0 = 20:22$ UTC for $\tau = 02:46:40$.

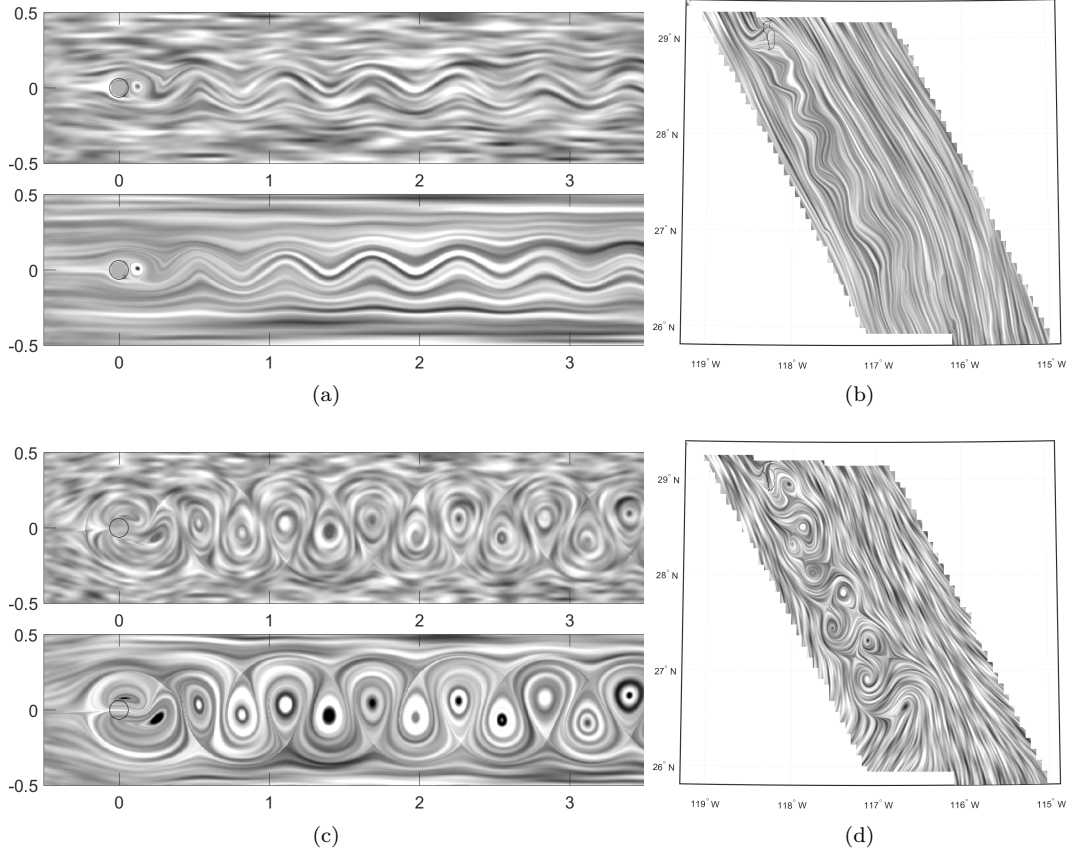


Figure 4: Line integral convolution for the original flows (a)–(b), and after subtraction of the ambient motion (c)–(d). The ambient motion describes how flow features are advected. After subtraction, flow features are revealed. In (a) and (c), we see the CYLINDER2D flow at time $t_0 = 10$ for $\tau = 0.2$ ((a) top), $\tau = 1.0$ ((a) bottom), $\tau = 0.1$ ((c) top) and $\tau = 0.5$ ((c) bottom). In (b) and (d), GUADALUPE at 18:57 UTC is shown.

370 grades the noise values along a streamline, where the length of the streamline is a user
 371 parameter. For pixels located nearby on the same streamline, the integration accumu-
 372 lates almost identical noise values, resulting in very similar gray values along the stream-
 373 line. Adjacent streamlines, however, sample an uncorrelated set of random values, re-
 374 sulting in a different gray value. It is important to note that the streamline should be
 375 arclength parameterized. If it were parameterized by the integration duration, too many
 376 identical noise values would be added once a streamline approaches a critical point or
 377 gets stuck at an obstacle, leading to noticeable artifacts and loss of visual contrast.

378 5.3 Discussion

379 The effectiveness of texture advectons depends on the patterns that are advected,
 380 for example, the size of the squares of a checkerboard pattern. The larger the patterns,
 381 the less localized information becomes visible. While the shape of the advected squares
 382 informs the reader whether a deformation occurred or not, the display of non-deformed
 383 black and white squares still grabs attention through the display of edges that do not
 384 carry a particular meaning.

385 Despite their popularity, line integral convolutions are limited to the display of stream-
 386 lines, making them unsuitable for the extraction of dynamical features in time-dependent
 387 flow. The LIC images plotted for a given timestep in Figs. 4a and 4b convey very sim-
 388 ilar information to the streamlines plotted in Fig. 2. Their main advantage is that they
 389 cover the entire domain and avoid the seeding problem of the streamlines. While some
 390 extensions have been proposed that integrate along pathlines (Han-Wei Shen & Kao, 1997),
 391 those are less frequently used. A more common alternative is to subtract the ambient
 392 velocity from the flow in order to separate features such as vortices from their movement.
 393 In the literature, a number of approaches can be found, including the subtraction of an
 394 average inflow velocity (Weinkauff et al., 2007), or the harmonic component of a Helmholtz
 395 decomposition (Bhatia et al., 2014) to separate external from internal flow behavior. Al-
 396 ternatively, the ambient velocity can be described as the velocity of an observer that moves
 397 with flow features such as vortices. Motivated by the seminal observation of Lugt (1979)
 398 that there is no single observer that can follow all flow features in the domain at once,
 399 Günther et al. (2017) searched for an observer locally that sees the vector field in an as-
 400 steady-as-possible way. The velocity field seen by this observer thereby becomes approx-
 401 imately steady, making the use of streamlines appropriate to reveal flow features. The
 402 result of such an unsteadiness minimization using the spatially-varying formulation of
 403 Baeza Rojo and Günther (2020) is shown in Fig. 4 (c)–(d), which now reveals the vor-
 404 tices. Similar optimizations have been done globally (Hadwiger et al., 2019) and on gen-
 405 eral manifolds (Rautek et al., 2021). The optimization of reference frames is numerically
 406 challenging, especially on measured data, as it requires accurate derivative estimates. In
 407 the following, we move on to feature-based methods that are derived from pathline be-
 408 havior.

409 6 Feature-based Methods

410 6.1 Lagrangian Coherent Structures

411 Fluid flows are a continuum of particles. In a flow, there are distinguished sets of
 412 particles, so-called material lines, that determine the behavior of the fluid. For a com-
 413 parative fluid flow analysis, those material lines are of high interest, since they divide
 414 the domain into regions with coherent behavior, which could be compared among given
 415 vector fields. For instance, such material lines enclose vortices or denote transport bar-
 416 riers, which are both important objects when studying transport and mixing. In the fluid
 417 dynamics literature, these structures are called Lagrangian coherent structures (LCS).
 418 Recently, Haller (2015) gave a comprehensive overview of the types of LCS and their ex-
 419 traction algorithms. We refer to Onu et al. (2015) for more details on LCS extraction
 420 techniques. LCS structures can be derived from variational principles, i.e., they are lines
 421 that maximize or minimize a certain behavior. Commonly, three types are distinguished:

- 422 • *Hyperbolic LCS* are material lines that repel or attract particles locally the strongest (Haller,
 423 2011). These lines act as transport barriers and are found by observing flow be-
 424 havior in forward and backward time.
- 425 • *Elliptic LCS* are the boundaries of vortices, which have been characterized as lines
 426 that bound coherent rotations (Haller et al., 2016), that show no stretching dur-
 427 ing advection (Serra & Haller, 2016), or that inhibit vorticity diffusion (Katsanoulis
 428 et al., 2019).
- 429 • *Parabolic LCS* are material lines along which material shearing is minimized (Farazmand
 430 et al., 2014), which identifies jet cores. In atmospheric flows, they have also been
 431 characterized as lines with maximal flow velocity (Kern et al., 2017).

432 In the following, we take a closer look at vortices and transport barriers, since those are
 433 the structures that can be found in Kármán vortex streets.

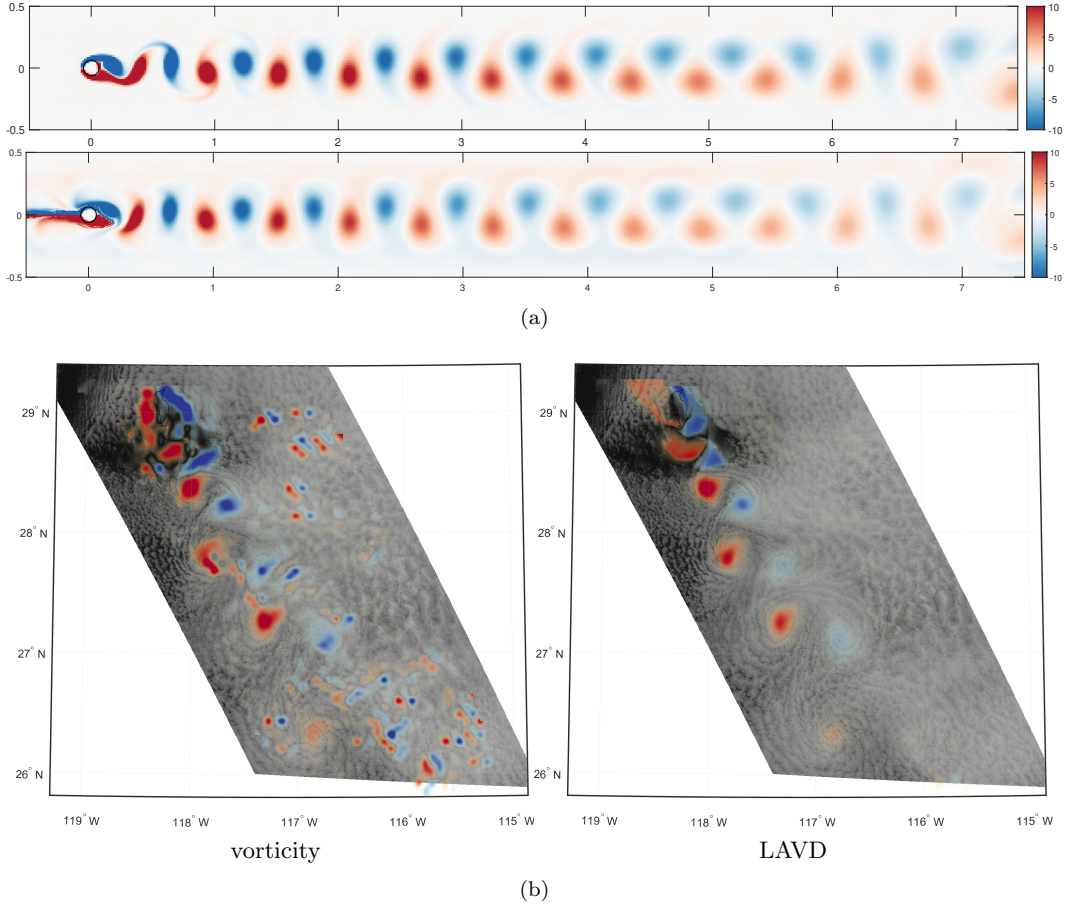


Figure 5: Comparison of vorticity, which is calculated per time slice, with its temporally-coherent extension named Lagrangian-averaged vorticity deviation (LAVD). In (a), the CYLINDER2D flow is visualized by calculating vorticity (top) at time $t_0 = 12$, and using LAVD (bottom) at $t_0 = 12$, $\tau = 2$, $U = 41 \times 41$ grid points. In (b), the GUADALUPE flow is depicted by vorticity (left) at 17:02 UTC and by LAVD (right) from $t_0 = 15:47$ UTC for duration $\tau = 02:46:40$ and $U = 21 \times 21$ grid points, which covers 252 km^2 .

434

6.2 Vortices

435

436

437

438

439

440

441

442

443

Vortex measures are categorized into region-based and line-based methods. Region-based methods return a scalar field that expresses how strong the vortical behavior is at a certain location. To extract vortices, a threshold needs to be applied, which is often not easy to set, since vortices decay over time or carry a varying amount of angular momentum throughout the domain. Line-based methods on the other hand return the so-called vortex coreline, which is the line that all other particles swirl around. In the following, we explain two of the most common vortex measures for two-dimensional flows. We refer to Günther and Theisel (2018) for a recent and comprehensive overview of vortex extraction techniques.

One of the most prominent region-based vortex measures is the vorticity scalar field $\omega(x, y)$

$$\omega(x, y) = \frac{\partial v(x, y)}{\partial x} - \frac{\partial u(x, y)}{\partial y} \quad (10)$$

For meteorological flows, we let $\omega(x, y)$ be the vorticity measured relative to the Earth’s rotation, which is then also referred to as *relative vorticity*. The sign of ω determines the rotation direction, whereas the magnitude relates to twice the angular velocity of a virtual tracer particle. It can be seen in Eq. (10) that the vorticity field requires an estimation of derivatives, which is challenging in noisy measurement data. It can be expected that the resulting vorticity scalar field contains patches of noise, which in fact are apparent in Fig. 5. Rather than spatially averaging the values to remove the noise, as was done in Horváth et al. (2020), it is more suitable to average vorticity values along a pathline over time. This way, long-living vortex structures are revealed and short-lived noise is removed. Vorticity ω is only Galilean invariant—i.e. invariant only in an inertial non-accelerating reference frame—because the rotation of an observer adds to the vorticity scalar, which is undesirable since ideally all observers should observe the feature in the same way. Fortunately, the difference between two spatially-neighboring vorticity values cancels the added observer rotation, making not only vorticity extrema, but also the deviation of relative vorticity—i.e., the difference to the local average vorticity—objective. Haller et al. (2016) proposed the Lagrangian-averaged vorticity deviation, which averages the vorticity deviations along pathlines:

$$\text{LAVD}(\mathbf{x}, t; \tau) = \int_t^{t+\tau} |\omega(\Phi_t^{s-t}(\mathbf{x}), s) - \omega_{avg}(\Phi_t^{s-t}(\mathbf{x}), s)| ds \quad (11)$$

444 where $\omega_{avg}(\mathbf{x}, t) = \frac{1}{|U(\mathbf{x})|} \int_{U(\mathbf{x})} \omega(\mathbf{x}, t) dV$ is the average vorticity in a local neighborhood U . LAVD is objective and locates temporally-coherent structures. For the CYLINDER2D flow in Fig. 5(a), LAVD (bottom) emphasizes locations that remain for a long time inside a vortex. Thus, the vortices in the immediate wake of the cylinder become more circular than with vorticity (top).
445
446
447
448

449 In the GUADALUPE flow, we not only see that LAVD removed the noise successfully, but the vortex locations are also well aligned with the circular cloud patterns. Moreover, the captured vortex decay is asymmetric: anticyclonic vorticity decreases significantly faster than cyclonic vorticity. Such contrast is detectable in the visual appearance of the vortices too, because anticyclonic eddies have less well-preserved spiral patterns than cyclonic eddies at the same downstream location. As discussed in Horváth et al. (2020), an asymmetric island wake is the expected behavior, predicted by both laboratory experiments and numerical simulations, which arises from the combined effects of Earth’s rotation and Guadalupe’s nonaxisymmetric shape resembling an inclined flat plate at low angle of attack. The good correspondence between the asymmetric LAVD field and the observed cloud structures indirectly confirms the fidelity of the fluid dynamics embedded in the measured wind field.
450
451
452
453
454
455
456
457
458
459
460

6.3 Material Boundaries

461 When releasing a small group of particles inside a finite-sized sphere, the small sphere is likely to deform under the action of advection over time. Locations at which a sphere elongates locally the strongest are part of a repelling hyperbolic LCS. The opposite attracting hyperbolic LCS are found by observing the transport behavior in backward time. In continuum mechanics, this local deformation is linearly approximated by the right Cauchy-Green deformation tensor:

$$\mathbf{C}(\mathbf{x}, t; \tau) = \frac{\partial \Phi_t^\tau(\mathbf{x})}{\partial \mathbf{x}}^T \frac{\partial \Phi_t^\tau(\mathbf{x})}{\partial \mathbf{x}} \quad (12)$$

The gradient of the flow map, which is numerically calculated by central differences, is multiplied with its transpose to make this deformation measure invariant under rotations of the observer. The largest eigenvalues of this tensor (λ_{max}) encode the strongest linear elongation. Introducing normalizations to account for the squaring of the gradient in Eq. (12), the exponential separation rate, and the continued growth over the duration τ , leads to the finite-time Lyapunov exponent (FTLE) (Shadden et al., 2005; Haller,

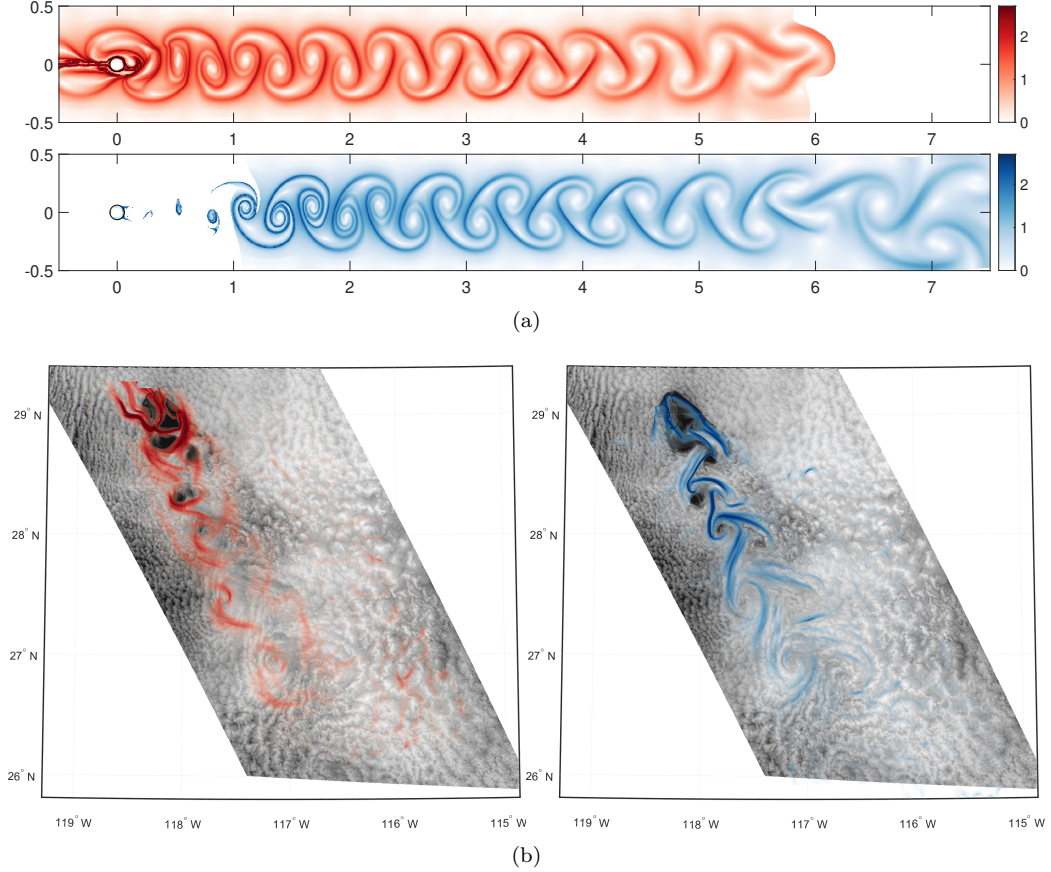


Figure 6: The finite-time Lyapunov exponent reveals attracting (backward FTLE, blue) and repelling (forward FTLE, red) material lines in the domain that strongly influence the passive transport of particles. In the CYLINDER2D, slice $t_0 = 10$ is shown with FTLE integration duration $\tau = 1.5$. The GUADALUPE flow is displayed at time $t_0 = 18:22$ UTC with an FTLE integration duration of $\tau = 02:46:40$ both forward and backward.

2001):

$$\text{FTLE}(\mathbf{x}, t; \tau) = \frac{1}{|\tau|} \ln \sqrt{\lambda_{\max}(\mathbf{C}(\mathbf{x}, t; \tau))} \quad (13)$$

462 Ridges in this scalar field are frequently used as approximations to hyperbolic LCS. Fig. 6
 463 depicts forward FTLE (repelling behavior) and backward FTLE (attracting behavior)
 464 in the CYLINDER2D and the GUADALUPE flows. Attracting FTLE ridges are computed
 465 by backward integration within a time span $[t - \tau, t]$, i.e., they reveal structures that
 466 have formed in the past up until the current time t . The alignment of the attracting FTLE
 467 ridges in the GUADALUPE flow with the cloud patterns shows that the transport dynam-
 468 ics of the satellite-measured wind field are in agreement with the observed organiza-
 469 tion of clouds. Repelling FTLE ridges are computed by forward integration within a time span
 470 $[t, t + \tau]$, i.e., they indicate regions that will show repelling behavior in the future. In
 471 a von-Kármán vortex street, the strongest repelling ridges (red) arise from particles that
 472 attract onto (or towards) an attracting FTLE ridge (blue), but will then separate in op-
 473 posite directions along the blue FTLE ridge, as the separating particles get curled up in
 474 different vortices. The red ridge line and the blue ridge line thereby separate vortex
 475 regions. In topological terms, the intersection of those red and blue ridge lines results
 476 in a bifurcation point.

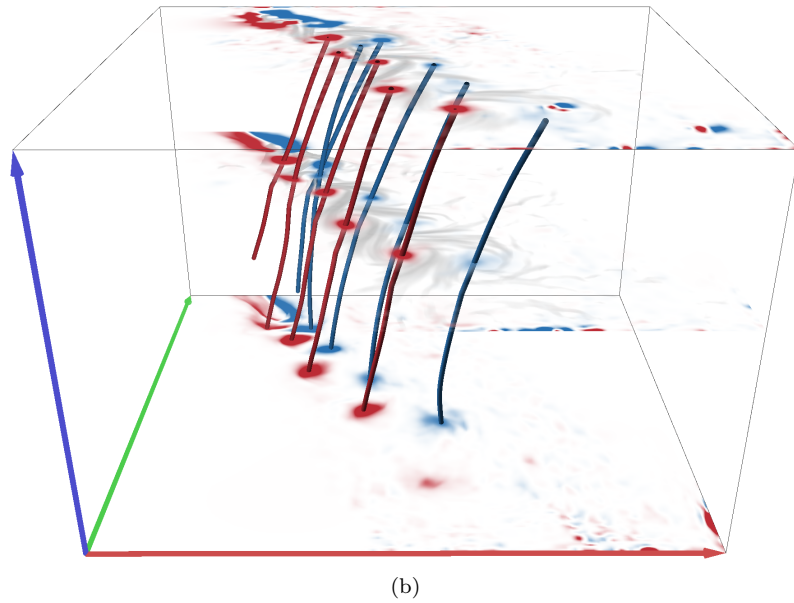
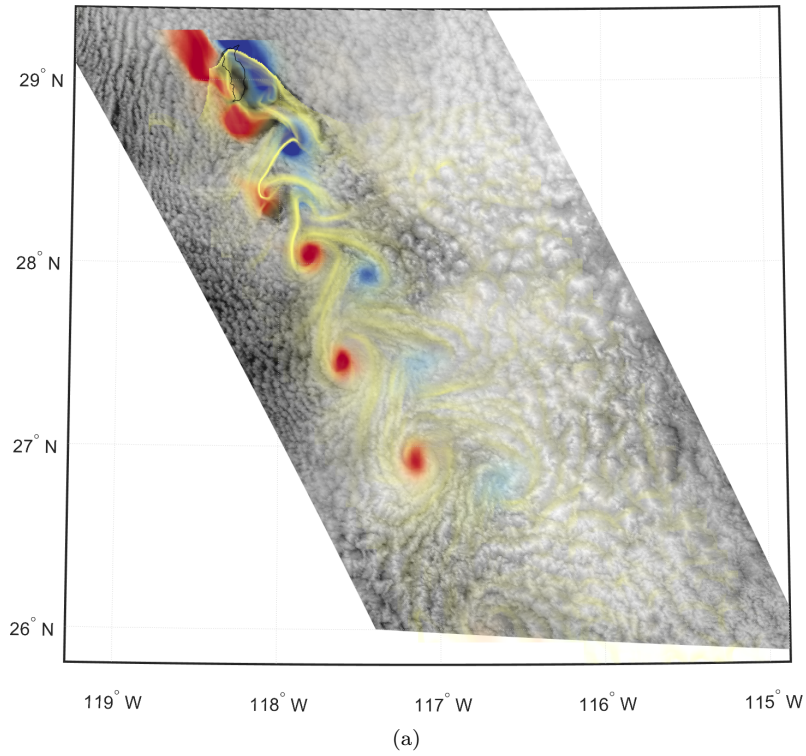


Figure 7: Feature-based quality assessment of the GUADALUPE velocity field obtained by cloud tracking. In (a), overlaying vortices (LAVD in red/blue) and attracting transport barriers (backward FTLE in yellow) on visible imagery shows the agreement of the retrieved fluid dynamical processes with the observed cloud patterns. Here, at $t_0 = 18:22$ UTC for an FTLE and LAVD integration duration of $\tau = 02:46:40$. In (b), a space-time mapping of the flow reveals temporally coherent vortex paths with FTLE time slices from bottom to top at 14:32, 19:22, and at 22:37 UTC.

6.4 Space-Time Mapping

Time-dependent 2D flows have three dependent variables: the position coordinates x and y , and the time t . A rather natural form to visualize a time-dependent flow is to visualize each time slice independently and play the time series as a video. This form of animation is suitable to show the instantaneous changes around the currently observed time slices, but is not very effective in communicating motions that occurred across larger time spans, such as the path of a vortex in our vortex street. For such a 2D time-dependent flow, we can lift the domain one dimension up by mapping the time to the third spatial dimension, which leads to a so-called *space-time* visualization. We will denote a coordinate in space-time with $\bar{\mathbf{x}} = (\mathbf{x}, t)$, which incidentally also describes a coordinate in the phase space of a particle, thus making this a space that captures all dimensions of the dynamical system. There are two common space-time velocity fields that can be derived from the unsteady vector field, see Theisel et al. (2004):

$$\bar{\mathbf{s}}(\bar{\mathbf{x}}) = \frac{d}{dt} \begin{pmatrix} x \\ y \\ t \end{pmatrix} = \begin{pmatrix} u(x, y, t) \\ v(x, y, t) \\ 0 \end{pmatrix} \quad \bar{\mathbf{p}}(\bar{\mathbf{x}}) = \frac{d}{dt} \begin{pmatrix} x \\ y \\ t \end{pmatrix} = \begin{pmatrix} u(x, y, t) \\ v(x, y, t) \\ 1 \end{pmatrix} \quad (14)$$

which differ in the rate of change of the last dimension, i.e., the time. The tangent curves in the field $\bar{\mathbf{s}}(\bar{\mathbf{x}})$ are streamlines, whereas the tangent curves of $\bar{\mathbf{p}}(\bar{\mathbf{x}})$ are pathlines. A direct visualization of the flow features in these two fields immediately shows streamline-oriented and pathline-oriented vector field topology. For fluid flows, we are primarily interested in $\bar{\mathbf{p}}(\bar{\mathbf{x}})$. Due to the mapping of the time axis to the third spatial dimension, the paths of vortices, later extracted as extremal lines of the LAVD field, become quickly apparent. For an introduction to the rendering and extraction of extremal features, we refer to Kindlmann et al. (2018).

In Fig. 7, the previously introduced feature extraction methods are used to assess the quality of the vector field that was reconstructed from measured cloud motion. In Fig. 7a, the visible band satellite image of the vortex street is overlaid with the elliptic LCS (in terms of LAVD) and attracting hyperbolic LCS (in terms of backward FTLE). We can clearly see that the emergence of patterns in the cloud field is constrained by and organized around the LCS, which provides strong evidence that the retrieved vector field exhibits the same fluid dynamical processes that the real-world clouds actually experienced. The space-time visualization in Fig. 7b further sheds light onto the temporal evolution of the vortices, with the blue axis denoting time. Not only can we see how the vortices interacted with each other, but we can also observe the temporal stability of the extracted paths, which can likewise be considered as a quality indicator.

6.5 Discussion

Derived features, such as region-based vortex measures or the finite-time Lyapunov exponent field as indicator for hyperbolic Lagrangian coherent structures, are not only useful for a qualitative visual comparison, but can also be useful for a feature-centered quantitative evaluation. In both flow visualization and fluid dynamics, two important properties have been recognized as essential characteristics that flow features should possess. First, the features should be seen by all rotating and translating observers in an equal manner, their motion notwithstanding, which is referred to as objectivity. Both LAVD and FTLE fulfill this property. Second, a Lagrangian coherent feature should—as the name suggests—be coherent when observed along pathlines over time. Thus, both LAVD and FTLE measure the fluid behavior over a certain time window. The length of this time window, thereby remains a crucial user parameter. A limitation of both LAVD and FTLE is that it is unclear where along the pathline the characteristic feature behavior was observed. For example, consider pathlines that stay close together most of the time and only separate strongly towards the end of the set time interval. This delayed separation is not immediately visible from the scalar field alone and is only revealed

513 when the parameter-dependence of the features is explored, cf. Sagristà et al. (2020) for
 514 parameter analysis tools. Alternatively, features could be extracted locally per time slice
 515 and joined afterwards in time to precisely determine the beginning and end of a feature’s
 516 life time. The latter motivates ongoing research on the temporally-local analysis of time-
 517 dependent vector field topology (Baeza Rojo & Günther, 2020), which could deliver an-
 518 other set of features useful for a comparative analysis of scalar and vector fields. This
 519 direction of research is left for future work.

520 7 Conclusions

521 With the advent of the latest generation geostationary imagers, such as ABI on GOES-
 522 R, satellite wind retrievals on the km and minute scale have become a reality. These high
 523 spatiotemporal-resolution winds enable the study of mesoscale geophysical flows and
 524 are also in increasing demand as input data for the ever-finer resolution operational fore-
 525 cast models. However, the visualization and validation—or at least consistency test—of
 526 these data sets is challenging and progress on these fronts will require moving beyond
 527 traditional techniques, such as gridpoint-based comparisons to radiosonde, aircraft, or
 528 reanalysis winds. To this end, we demonstrated advanced visualization and dynamical
 529 system analysis tools through the example of a high-resolution GOES-16 wind data set
 530 that captures an atmospheric Kármán vortex street in the lee of Guadalupe.

531 The fluid dynamics of the reconstructed vector field should give rise to flow fea-
 532 tures that correlate with the observed mesoscale cloud patterns, since those patterns are
 533 the result of a fluid dynamical evolution. We discussed the advantages and disadvantages
 534 of various visualization approaches. Direct methods such as arrow plots are able to show
 535 noise in the data, but are obscured by the ambient motion of features in time-dependent
 536 flow. Geometry-based methods (integral curves) require careful seeding and are primar-
 537 ily useful for qualitative analysis, and when shown in combination with an underlying
 538 scalar field that makes use of the non-occluded spaces. Texture-based techniques such
 539 as texture advection and line integral convolution convey information more densely, but
 540 especially LIC must be used with care, since it displays streamlines, which are non-physical
 541 unless observed in a suitable unsteadiness-minimizing reference frame. Feature-based meth-
 542 ods such as LAVD and FTLE, however, reveal Lagrangian Coherent Structures that drive
 543 the fluid dynamical processes. Both of the latter approaches are objective and incorpo-
 544 rate the desirable temporal coherence of the features in question.

545 The LAVD and FTLE fields computed from the GOES-16 winds align well with
 546 the observed mushroom cloud patterns of the vortex street, indirectly validating the satel-
 547 lite retrievals. In the current study, the comparison of observed and derived structures
 548 was qualitative (visual) only, but it is not difficult to put the comparison on a quanti-
 549 tative basis by applying feature-based spatial forecast verification methods. These meth-
 550 ods operate precisely on the type of coherent objects that are represented by the Lagrangian
 551 Coherent Structures of the flow. The FTLE ridges can be extracted from both observed
 552 and simulated wind fields and then quantitatively compared by for instance the SAL tech-
 553 nique (Wernli et al. (2008)), which assesses the structure (size and shape), amplitude,
 554 and location of the identified objects. Other quantitative metrics could also be derived
 555 based on the presence and distance of vortices and transport barriers. In the next step,
 556 we plan to evaluate the performance of numerical simulations of the Guadalupe vortex
 557 street and their sensitivity to the used boundary layer scheme based on such feature-centered
 558 quality metrics. In principle, Lagrangian coherent structures reveal the fluid dynamical
 559 processes not only in 2D, but also in 3D flow. While it is a challenging problem to re-
 560 cover 3D wind vectors from observations, for example from multi-layered clouds, the fluid
 561 dynamical processes of model data could similarly be studied by the methods discussed
 562 in this paper, for example for air quality forecasting such as volcanic ash plumes or smoke
 563 plumes from wild fires.

Acknowledgments

The work of T. Günther was supported by the Swiss National Science Foundation (SNSF) Ambizione grant no. PZ00P2.180114. The work of A. Horváth was supported by German Federal Ministry of Education and Research (BMBF) project HD(CP)2 (contract O1LK1505D) and by Deutsche Forschungsgemeinschaft (DFG) project VolImpact/VolPlume (contract BU 2253/7-1). With this work we contribute to the Cluster of Excellence “CLICCS—Climate, Climatic Change, and Society” funded by DFG (EXC 2037, Project Number 390683824), and to the Center for Earth System Research and Sustainability (CEN) of Universität Hamburg.

Data Availability

The GOES-16 ABI L1b radiances are available from the NOAA Comprehensive Large Array-data Stewardship System (CLASS) archive (<https://www.avl.class.noaa.gov>). The high-resolution GOES-16 wind retrievals are available from the Zenodo data repository (<https://doi.org/10.5281/zenodo.3534276>). The code to reproduce the images in the paper, as well as the data can be found online at <https://github.com/tobguent/vislcs-guadalupe>.

References

- Baeza Rojo, I., & Günther, T. (2020). Vector field topology of time-dependent flows in a steady reference frame. *IEEE Transactions on Visualization and Computer Graphics*, *26*(1), 280-290. doi: 10.1109/TVCG.2019.2934375
- Bhatia, H., Pascucci, V., Kirby, R. M., & Bremer, P.-T. (2014). Extracting features from time-dependent vector fields using internal reference frames. *Computer Graphics Forum*, *33*(3), 21-30. doi: <https://doi.org/10.1111/cgf.12358>
- Borgo, R., Kehrer, J., Chung, D. H. S., Maguire, E., Laramee, R. S., Hauser, H., . . . Chen, M. (2013). Glyph-based Visualization: Foundations, Design Guidelines, Techniques and Applications. In M. Sbert & L. Szirmay-Kalos (Eds.), *Eurographics 2013 - state of the art reports*. The Eurographics Association. doi: 10.2312/conf/EG2013/stars/039-063
- Bresky, W., Daniels, J., & Wanzong, S. (2012). New methods toward minimizing the slow speed bias associated with atmospheric motion vectors. *Journal of Applied Meteorology and Climatology*, *51*(12), 2137–2151. doi: 10.1175/JAMCD110234.1
- Bujack, R., & Middel, A. (2020). State of the art in flow visualization in the environmental sciences. *Environmental Earth Sciences*, *79*(2), 1–10.
- Cabral, B., & Leedom, L. (1993). Imaging vector fields using line integral convolution. *Computer Graphics (Proc. SIGGRAPH)*, *27*, 263-272.
- Chen, Y., Cohen, J., & Krolík, J. (2007). Similarity-guided streamline placement with error evaluation. *IEEE Transactions on Visualization and Computer Graphics*, *13*, 1448-1455.
- Chopra, K. P., & Hubert, L. F. (1965). Mesoscale eddies in wakes of islands. *Journal of the Atmospheric Sciences*, *22*(6), 652–657. doi: 10.1175/15200469(1965)022%3C0652:MEIWOI%3E2.0.CO;2
- Cimbala, J. M., Nagib, H. M., & Roshko, A. (1988). Large structure in the far wakes of two-dimensional bluff bodies. *Journal of Fluid Mechanics*, *190*, 265–298. doi: 10.1017/S0022112088001314
- Daniels, J., Bresky, W., Wanzong, S., Velden, C., & Berger, H. (2010). *Goes-r advanced baseline imager (abi) algorithm theoretical basis document for derived motion wind*. GOES-R Program Office. Retrieved from https://www.star.nesdis.noaa.gov/goesr/documents/ATBDs/Baseline/ATBD_GOESR_Winds_v3.1_Feb2019.pdf
- Farzmand, M., Blazeovski, D., & Haller, G. (2014). Shearless transport barriers in unsteady two-dimensional flows and maps. *Physica D: Nonlinear Phenomena*,

- 278, 44–57.
- 616 Günther, T., Gross, M., & Theisel, H. (2017). Generic objective vortices for flow
617 visualization. *ACM Transactions on Graphics (Proc. SIGGRAPH)*, 36(4),
618 141:1–141:11.
- 619 Günther, T., Gross, M., & Theisel, H. (2017, July). Generic objective vortices for
620 flow visualization. *ACM Trans. Graph. (Proc. SIGGRAPH)*, 36(4). doi: 10
621 .1145/3072959.3073684
- 622 Günther, T., & Baeza Rojo, I. (2021). Introduction to vector field topology. In *Topo-
623 logical methods in data analysis and visualization vi*. Springer.
- 624 Günther, T., & Theisel, H. (2018). The state of the art in vortex extraction. *Com-
625 puter Graphics Forum*, 37(6), 149–173. doi: 10.1111/cgf.13319
- 626 Günther, T., Theisel, H., & Gross, M. (2017). Decoupled Opacity Optimization
627 for Points, Lines and Surfaces. *Computer Graphics Forum*. doi: 10.1111/cgf
628 .13115
- 629 Hadwiger, M., Mlejnek, M., Theußl, T., & Rautek, P. (2019). Time-dependent flow
630 seen through approximate observer killing fields. *IEEE Transactions on Visu-
631 alization and Computer Graphics (Proceedings IEEE Scientific Visualization
632 2018)*, 25(1), 1257–1266.
- 633 Haller, G. (2001, March). Distinguished material surfaces and coherent structures in
634 three-dimensional fluid flows. *Physica D: Nonlinear Phenomena*, 149(4), 248–
635 277. doi: 10.1016/S0167-2789(00)00199-8
- 636 Haller, G. (2011). A variational theory of hyperbolic Lagrangian coherent structures.
637 *Physica D: Nonlinear Phenomena*, 240(7), 574–598.
- 638 Haller, G. (2015). Lagrangian coherent structures. *Annual Review of Fluid Mechan-
639 ics*, 47, 137–162.
- 640 Haller, G., Hadjighasem, A., Farazmand, M., & Huhn, F. (2016). Defining coherent
641 vortices objectively from the vorticity. *Journal of Fluid Mechanics*, 795, 136–
642 173.
- 643 Han-Wei Shen, & Kao, D. L. (1997). Uffic: a line integral convolution algorithm
644 for visualizing unsteady flows. In *Proceedings. visualization '97 (cat. no.
645 97cb36155)* (p. 317–322). doi: 10.1109/VISUAL.1997.663898
- 646 Heinze, R., Raasch, S., & Etling, D. (2012). The structure of kármán vortex streets
647 in the atmospheric boundary layer derived from large eddy simulation. *Meteo-
648 rologische Zeitschrift*, 21(3), 221–237. doi: 10.1127/09412948/2012/0313
- 649 Holmlund, K., Velden, C. S., & Rohn, M. (2001). Enhanced automated quality
650 control applied to high-density satellite winds. *Monthly Weather Review*, 129,
651 517–529. doi: 10.1175/1520-0493(2001)129,0517:EAQCAT.2.0.CO;2
- 652 Horváth, Á. (2013). Improvements to misr stereo motion vectors. *Journal of Geo-
653 physical Research: Atmospheres*, 118, 5600–5620. doi: 10.1002/jgrd.50466
- 654 Horváth, Á., Bresky, W., Daniels, J., Vogelzang, J., Stoffelen, A., Carr, J., ...
655 Buehler, S. A. (2020). Evolution of an atmospheric kármán vortex street
656 from high-resolution satellite winds: Guadalupe island case study. *Jour-
657 nal of Geophysical Research: Atmospheres*, 125(4), e2019JD032121. doi:
658 10.1029/2019JD032121
- 659 Hubert, L. F., & Krueger, A. F. (1962). Satellite pictures of mesoscale eddies.
660 *Monthly Weather Review*, 90(11), 457–463. doi: 10.1175/15200493(1962)090%
661 3C0457:SPOME%3E2.0.CO;2
- 662 Jobard, B., & Lefer, W. (1997). Creating evenly-spaced streamlines of arbitrary
663 density. *Proc. Eurographics Workshop on Visualization in Scientific Comput-
664 ing*, 7, 45–55.
- 665 Katsanoulis, S., Farazmand, M., Serra, M., & Haller, G. (2019). Vortex bound-
666 aries as barriers to diffusive vorticity transport in two-dimensional flows. *arXiv
667 preprint arXiv:1910.07355*.
- 668 Kern, M., Hewson, T., Sadlo, F., Westermann, R., & Rautenhaus, M. (2017). Ro-
669 bust detection and visualization of jet-stream core lines in atmospheric flow.
- 670

- 671 *IEEE transactions on visualization and computer graphics*, 24(1), 893–902.
- 672 Kindlmann, G., Chiw, C., Huynh, T., Gyulassy, A., Reppy, J., & Bremer, P.-T.
673 (2018). Rendering and extracting extremal features in 3d fields. *Computer*
674 *Graphics Forum*, 37(3), 525–536. doi: <https://doi.org/10.1111/cgf.13439>
- 675 Laidlaw, D. H., Kirby, R. M., Jackson, C. D., Davidson, J. S., Miller, T. S., da Silva,
676 M., ... Tarr, M. J. (2005). Comparing 2d vector field visualization meth-
677 ods: A user study. *IEEE TRANSACTIONS ON VISUALIZATION AND*
678 *COMPUTER GRAPHICS*, 11(1), 59–70. doi: 10.1109/TVCG.2005.4
- 679 Lugt, H. J. (1979). The dilemma of defining a vortex. In U. Müller, K. G. Roes-
680 ner, & B. Schmidt (Eds.), *Recent developments in theoretical and experimental*
681 *fluid mechanics: Compressible and incompressible flows* (pp. 309–321). Berlin,
682 Heidelberg: Springer Berlin Heidelberg. doi: 10.1007/978-3-642-67220-0_32
- 683 Lyons, W. A., & Fujita, T. (1968). Mesoscale motions in oceanic stratus as revealed
684 by satellite data. *Monthly Weather Review*, 96(5), 304–314. doi: 10.1175/
685 15200493(1968)096<0304:MMIOSA>2.0.CO;2
- 686 MacCormack, R. W. (2002). The effect of viscosity in hypervelocity impact
687 cratering. In *Frontiers of computational fluid dynamics 2002* (p. 27–43).
688 Retrieved from [https://www.worldscientific.com/doi/abs/10.1142/](https://www.worldscientific.com/doi/abs/10.1142/9789812810793_0002)
689 [9789812810793_0002](https://www.worldscientific.com/doi/abs/10.1142/9789812810793_0002) doi: 10.1142/9789812810793_0002
- 690 Mattausch, O., Theußl, T., Hauser, H., & Gröller, E. (2003). Strategies for inter-
691 active exploration of 3D flow using evenly-spaced illuminated streamlines. In
692 *Proc. spring conference on computer graphics (ssc)* (pp. 213–222). ACM. doi:
693 <http://doi.acm.org/10.1145/984952.984987>
- 694 McLoughlin, T., Laramee, R. S., Peikert, R., Post, F. H., & Chen, M. (2010,
695 September). Over two decades of integration-based, geometric flow visual-
696 ization. *Computer Graphics Forum*, 29(6), 1807–1829.
- 697 Nunalee, C. G., & Basu, S. (2014). On the periodicity of atmospheric von kármán
698 vortex streets. *Environmental Fluid Mechanics*, 14(6), 1335–1355. doi: 10
699 .1007/s1065201493409
- 700 Nunalee, C. G., Horváth, Á., & Basu, S. (2015). High-resolution numerical modeling
701 of mesoscale island wakes and sensitivity to static topographic relief data. *Geo-*
702 *scientific Model Development*, 8(8), 2645–2653. doi: 10.5194/gmd826452015
- 703 Onu, K., Huhn, F., & Haller, G. (2015). LCS tool: a computational platform for La-
704 grangian coherent structures. *Journal of Computational Science*, 7, 26–36.
- 705 Popinet, S. (2003). Gerris: a tree-based adaptive solver for the incompressible euler
706 equations in complex geometries. *Journal of Computational Physics*, 190(2),
707 572–600.
- 708 Rautek, P., Mlejnek, M., Beyer, J., Troidl, J., Pfister, H., Theußl, T., & Hadwiger,
709 M. (2021). Objective observer-relative flow visualization in curved spaces
710 for unsteady 2d geophysical flows. *IEEE Transactions on Visualization and*
711 *Computer Graphics (Proceedings IEEE Scientific Visualization 2020)*, 27(2),
712 to appear.
- 713 Sagristà, A., Jordan, S., & Sadlo, F. (2020). Visual analysis of the finite-time lya-
714 punov exponent. *Computer Graphics Forum (Proc. EuroVis)*, 39(3), 331–342.
715 doi: <https://doi.org/10.1111/cgf.13984>
- 716 Sane, S., Bujack, R., Garth, C., & Childs, H. (2020). A survey of seed placement
717 and streamline selection techniques. *Computer Graphics Forum*, 39(3), 785–
718 809. doi: <https://doi.org/10.1111/cgf.14036>
- 719 Serra, M., & Haller, G. (2016). Objective eulerian coherent structures. *Chaos: An*
720 *Interdisciplinary Journal of Nonlinear Science*, 26(5), 053110.
- 721 Shadden, S. C., Lekien, F., & Marsden, J. E. (2005). Definition and properties of
722 Lagrangian coherent structures from finite-time Lyapunov exponents in two-
723 dimensional aperiodic flows. *Physica D: Nonlinear Phenomena*, 212(3–4),
724 271–304. doi: 10.1016/j.physd.2005.10.007
- 725 Theisel, H., Weinkauff, T., Hege, H.-C., & Seidel, H.-P. (2004). Stream line and path

- 726 line oriented topology for 2d time-dependent vector fields. In *Proc. ieee visual-*
727 *ization 2004* (pp. 321–238).
- 728 Truesdell, C., & Noll, W. (1965). *The nonlinear field theories of mechanics*. Hand-
729 buch der Physik, Band III/3, e by Flugge, S., (ed.) , Springer-Verlag, Berlin.
- 730 Van Dyke, M. (1982). An album of fluid motion.
- 731 Vogelzang, J., Stoffelen, A., Lindsley, R. D., Verhoef, A., & Verspeek, J. (2017).
732 The ascats 6.25 km wind product. *IEEE Journal of Selected Topics in Ap-*
733 *plied Earth Observations and Remote Sensing*, 10(5), 2321–2331. doi:
734 10.1109/JSTARS.2016.2623862
- 735 Weinkauff, T., Hege, H.-C., & Theisel, H. (2012). Advected tangent curves: A gen-
736 eral scheme for characteristic curves of flow fields. *Computer Graphics Forum*,
737 31(2pt4), 825–834. doi: <https://doi.org/10.1111/j.1467-8659.2012.03063.x>
- 738 Weinkauff, T., Sahner, J., Theisel, H., & Hege, H. (2007). Cores of swirling particle
739 motion in unsteady flows. *IEEE Transactions on Visualization and Computer*
740 *Graphics*, 13(6), 1759–1766. doi: 10.1109/TVCG.2007.70545
- 741 Wernli, H., Paulat, M., Hagen, M., & Frei, C. (2008). Sal—a novel quality measure
742 for the verification of quantitative precipitation forecasts. *Monthly Weather*
743 *Review*, 136(11), 4470–4487. doi: 10.1175/2008MWR2415.1
- 744 Ye, X., Kao, D., & Pang, A. (2005). Strategy for seeding 3D streamlines. *IEEE*
745 *Visualization Conference*, 471–478. doi: [http://doi.ieeecomputersociety.org/10](http://doi.ieeecomputersociety.org/10.1109/VIS.2005.92)
746 [.1109/VIS.2005.92](http://doi.ieeecomputersociety.org/10.1109/VIS.2005.92)
- 747 Young, G. S., & Zawislak, J. (2006). An observational study of vortex spacing in is-
748 land wake vortex streets. *Monthly Weather Review*, 134(8), 2285–2294. doi: 10
749 [.1175/MWR3186.1](https://doi.org/10.1175/MWR3186.1)
- 750 Yu, H., Wang, C., Shene, C.-K., & Chen, J. (2012). Hierarchical streamline bun-
751 dles. *IEEE Transactions on Visualization and Computer Graphics*, 18(8),
752 1353–1367. doi: 10.1109/TVCG.2011.155